ORIGINAL PAPER

Real-Time Measurement of Mechanical Behavior of Granite During Heating–Cooling Cycle: A Mineralogical Perspective

Chengkang Mo[1] · Junliang Zhao[2] · Dongxiao Zhang[2]

Abstract

Changes in mechanical properties of rocks at high temperatures are significant to various scientific and engineering problems, such as efficient exploration in enhanced geothermal systems (EGS) and rock mass stability in radioactive waste disposal. However, a comprehensive understanding of changes in rock mechanical behaviors at high temperatures and corresponding mechanisms, especially granites, remains unclear, which calls for the examination of micromechanical properties of the constituent minerals. This work investigates four representative minerals in granites, including quartz, plagioclase, amphibole, and biotite. The micromechanical properties of these minerals in the heating–cooling cycle were characterized in real time by using the nanoindentation technique. The morphology of samples was observed not only under real-time cyclic heating–cooling conditions, but also after thermal treatment. Subsequently, changes in structure of the minerals at elevated temperatures based on X-ray diffraction (XRD) were studied. Thermogravimetric analysis coupled with Fourier's transform infrared spectroscopy (TG-FTIR) was performed to examine physio-chemical alterations of minerals at high temperatures. The experimental results revealed that the reduced modulus and hardness of quartz decreased during heating and subsequently increased during cooling. During the heating–cooling cycle, the hardness of plagioclase varied similarly to that of quartz, but its reduced modulus increased up to approximately 300 °C followed by a decrease during heating. Unlike the net decrease of modulus of quartz after exposure to the heating–cooling cycle, feldspar showed a net increase of modulus. The micromechanical properties of biotite were found to rise significantly during heating, followed by a decrease during cooling. XRD results suggested the alteration of mineral structure, including spacing of lattice planes, crystallinity, and phase transitions, which controlled the above changes in mechanical behaviors of quartz, amphibole, and plagioclase. However, the aperture of open cracks along the cleavage in biotite determined its micromechanical properties during heating and cooling. Thermally-induced microcracks were observed during heating; whereas, closure of pre-existing cracks and initiation of microcracks were found during cooling. The real-time measured micromechanical properties of minerals could relate to the macromechanical behaviors of rocks under heating–cooling conditions based on thermally-induced microcracks.

Highlights

- Micromechanical properties of constituent minerals in granites during heating-cooling cycles are investigated.

✉ Junliang Zhao
  zhaojl3@sustech.edu.cn

✉ Dongxiao Zhang
  zhangdx@sustech.edu.cn

  Chengkang Mo
  mck@pku.edu.cn

1 BIC-ESAT, ERE, and SKLTCS, College of Engineering, Peking University, No.5 Yiheyuan Road Haidian District, Beijing 100871, People's Republic of China

2 Shenzhen Key Laboratory of Natural Gas Hydrates, Southern University of Science and Technology, 1088 Xueyuan Avenue, Shenzhen 518055, People's Republic of China

- Changes in the crystal structure of quartz, plagioclase, and amphibole control their micromechanical behaviors during the heating-cooling condition.
- The thermally-induced cracks along the cleavage determine the micromechanical parameters of biotite.

Keywords Nanoindentation · Heating and cooling cycle · Real-time · Crystalline rock · Mineral structure

1 Introduction

An understanding of thermal effects on the mechanical behavior of rocks is important for geological science and underground engineering applications, such as enhanced geothermal systems (EGS), thermal drilling, and high-level radioactive waste disposal (HLW). In natural geothermal reservoirs, rocks are subjected to continuous heating conditions, and the preheating test conditions can not reproduce the in situ temperature conditions (Shao et al. 2015; Zhou et al. 2020). During EGS development, cold working fluid is injected into high-temperature hot dry rock (HDR) reservoirs with a temperature of $100 - 400\,°C$ (Tomac and Sauter 2018), resulting in thermally-induced cracks to enhance heat recovery. Moreover, rocks are heated to high temperatures in thermal drilling, especially in geological formations with hard rock, leading to thermal cracking. In addition, surrounding rocks can be heated due to radioactive decay in HLW. Therefore, the results of experimental researches performed on preheated specimens at room temperature are insufficient to characterize the essential mechanical behaviors of rock at high temperature in the above geological science and engineering applications. Furthermore, granite, as a composite material, is composed of various minerals as described in detail below, which necessitates the investigation of mechanical behaviors of minerals under this heating–cooling condition.

The underlying mechanism of mechanical properties changes during thermal loading, in general, is the build-up of thermal stress. The accumulation of thermal stress resulting from the thermal expansion mismatch of minerals during heating contributes to thermal microcracking (Kranz 1983). Moreover, temperature-gradient-induced thermal stress exceeding the mechanical strength of mineral grains results in the formation thermal cracks (Jansen et al. 1993). To better understand thermal effects on mechanical behaviors of granites, rocks samples were conventionally characterized at macroscale under three types of thermal conditions: (1) thermal treatment, i.e., the prepared rock samples were heated to the target temperature, maintained at the target temperature, and then cooled down to room temperature (RT); (2) cyclic thermal treatment, in which the rock samples were thermally treated [the same as (1)] at least twice prior to mechanical characterization; and (3) real-time characterization under heating and cooling. The mechanical tests of rock samples were carried out in real time under heating or cooling conditions. In the first type, the thermal influence of mechanical properties has been revealed by Young's modulus, compressive strength, and tensile strength via uniaxial, triaxial, and tension tests, respectively. The variation of mechanical properties of rocks with temperature was affected by various factors, such as initial pore structure, grain size, mineral composition, mineral texture, and water content. The experimental results showed the above mechanical properties of granites generally reduced with thermal treatment temperature. Some studies, however, indicated that these mechanical properties did not decrease monotonically. Specifically, the mechanical properties increased at first and then decreased beyond a threshold temperature (Zhang et al. 2020). Tian et al. (2020) found that the effect of thermal treatment on mechanical and transport properties was divided into three stages: (1) $T = 150\,°C$: porosity, peak strength and elastic modulus increased with temperatures; (2) $T = 300\,°C$: porosity increased with peak strength, however, the elastic modulus remained almost unchanged; (3) $T > 450\,°C$: porosity generally increased with temperatures, while peak strength and elastic modulus both decreased.

Yang et al. (2017) analyzed the deformation mechanism of granite after various thermal treatment temperatures and concluded that the brittle fracture dominated at $25\,°C$ to $600\,°C$, while thermal damage controlled the ductile fracture process of granite at 70 to $800\,°C$. Wong et al. (2020) concluded that three primary mechanisms resulted in rock-strengthening after thermal treatment under $200\,°C$: (1) closure of pre-existing microcracks; (2) thermally-induced microcracks; and (3) water-related changes. However, rocks may subject to thermal treatment repeatedly, such as in long-time exploration of EGS. Consequently, many studies were conducted under the second type of condition. When rocks are exposed to cyclic thermal treatment, the mechanical properties of granites were found to decrease significantly during the first several thermal cycles (Zhu et al. 2021, 2020). The intensity of thermal damage increased with temperature (Wu et al. 2019), and the ductility of granites enhanced as temperature and thermal cycles increased (Yin et al. 2019). Nevertheless, the thermally-treated samples may not correctly reproduce the in-situ temperature conditions. For example, rocks in HLW storage sites and natural geothermal reservoirs are exposed to continuous heating

conditions. Therefore, investigations performed under the third thermal conditions, i.e., real-time measurement under heating and cooling conditions, are necessary. The real-time mechanical behaviors of rocks under high temperatures were different from those exposed to thermal treatment. When measured in real time, granites under heating conditions exhibited higher compressive strength (Ma et al. 2020; Yin et al. 2016) and were more ductile (Ma et al. 2020). Thermal cracks can be observed both in the heating and cooling processes (Zhang et al. 2020). Zhang et al. (2020) reported that the combination of irreversible thermally-induced cracks in heating and compressive stress led to cooling damage. In real-time acoustic emission monitoring and ultrasonic velocity measurements under the cyclic heating condition, Griffiths et al. (2018) discovered that the thermal microcracks of granites increased with temperature; meanwhile, initiation of thermal microcracks, or friction on microcrack surfaces, were found during cooling.

Since granite is a complex and heterogenous composite material, its macroscopic mechanical behaviors were determined by constituent minerals (Vázquez et al. 2015). For instance, harder minerals, such as quartz, can bear more crushing than biotite, which was prone to deflect and terminate cracks (Ghasemi et al. 2020). Among various constituents in rocks, some play a leading role in the mechanical properties at macroscale under thermal effects. After thermal treatment, quartz and calcite were found to be the predominant minerals controlling rock physicomechanical properties (Tiskatine et al. 2016). However, Chen et al. (2017) found that clay-like minerals, such as biotite and phlogopite affected the mechanical properties of granites dominantly. Therefore, characterizing thermal influence on the minerals of granites at microscale is significant for a better understanding of its corresponding macroscopic mechanical behaviors. Previous works showed that different minerals exhibited differing temperature-dependent mechanical properties. Quartz crystal transformed at approximately 573 °C ($\alpha - \beta$ phase transition) (Bragg and Gibbs 1925; Gibbs 1925; Tucker et al. 2001), resulting from its crystal structure changes, with elastic constants exhibiting an extreme dip near the transitional temperature (Kimizuka et al. 2003). The molecular dynamics (MD) simulation results indicated that the bulk moduli of muscovite crystal decreased with temperature (Teich-McGoldrick et al. 2012). The Vickers hardness of feldspars as a single crystal decreased with temperature (Huang et al. 1985). Natural minerals within rocks may not be perfect, containing various defects and inclusions (Luo et al. 2021). As a consequent, it is essential to in-situ characterize the mechanical properties of minerals within bulk rock samples, except for a single mineral crystal. Using the nanoindentation technique, Maruvanchery and Kim (2020) observed that the elastic modulus and

hardness of rock-forming minerals (quartz, plagioclase, k-feldspar, dolomite, and calcite) and mineral-to-mineral contacts reduced in thermally-treated sandstone specimens due to thermally-induced microcracks; whereas, the opposite occurred in the case of kaolinite. Li et al. (2020) concluded that the Young's modulus and hardness of feldspar in high-temperature-treated granites decreased significantly beyond the threshold temperature of 300 °C.

However, few studies were reported to characterize in real time thermal effects on micromechanical properties of constituent minerals within rocks under heating and cooling conditions. Furthermore, the effect of crystal structural variations on micromechanical properties measured in real time during heating and cooling conditions lacks systematic investigation. In this study, the technique of nanoindentation (also known as depth-sensing indentation or instrumented indentation) was used to examine the micromechanical properties of minerals in granites, and the morphology of the thermally-treated samples was determined by scanning electron microscope (SEM) and optical microscope. To further determine sample morphology in real time under heating and cooling conditions , observation tests were carried out by using an environmental scanning electron microscope (ESEM) equipped with a hot stage. In addition, to better understand the underlying mechanism of thermal influence on mechanical behaviors, an X-ray diffraction (XRD) experiment was conducted to investigate real-time changes in the structure of minerals under heating, and mass loss and mineralogical reactions during the heating process were analyzed through thermogravimetric analysis coupled with Fourier transform infrared spectroscopy (TG-FTIR) tests.

2 Materials and Methods

In this part, the source of samples is provided. In addition, the mineral composition of the sample was determined based on the combination of XRD and the advanced mineral analysis and characterization system (AMICS, Bruker).

**Table 1** The basic mechanical and physical properties of samples

Property	Value
Uniaxial compressive strength (GPa)	152.992 ± 59.36
Young's modulus (GPa)	20.18 ± 7.18
Poisson's ratio (-)	0.24 ± 0.22
Peak strain (%)	1.00 ± 0.066
Density (g cm^{-3})	2.81 ± 0.02

2.1 Sample Preparations and Mineral Composition

Granite samples were an HDR geothermal formation outcrop quarried from the Gonghe Basin in Qinghai Province, China. The basic mechanical and physical properties of the samples are listed in Table 1 (Appendix A gives the detailed test method). Specimens with the size of $(7 \times 7 \times 1)$ mm^3 were cut from the rock blocks. Afterward, the upper surfaces were ground mechanically (EM TXP, Leica) followed by argon ion milling (EM TIC 3X, Leica) to reduce surface roughness, which is essential for nanoindentation tests and microscopic observation under scanning electron microscopy (SEM).

An XRD experiment was conducted to qualitatively identify mineral composition. First, the granite block samples were comminuted and pulverized to powder of no more than 100 mesh (diameter ≤ 0.15mm). Then, the diffractograms were recorded using copper K_α (CuK_α) radiation with a wavelength 1.5406 Å (X-Pert3 Powder, PANalytical) operated at 40 kV and 40 mA. The scanning angle of 2θ ranged from 5 to 90° with a scanning speed of 5°/min.

Since the nanoindentation test requires high-precision positioning, the AMICS system was utilized to better identify the mineral composition of the tested samples at microscale. The AMICS system can collect mineral distribution maps by incorporating backscattered electrons (BSE), energy-dispersive X-ray spectroscopy (EDS), and an automatic phase-matching algorithm (Bruker 2021).
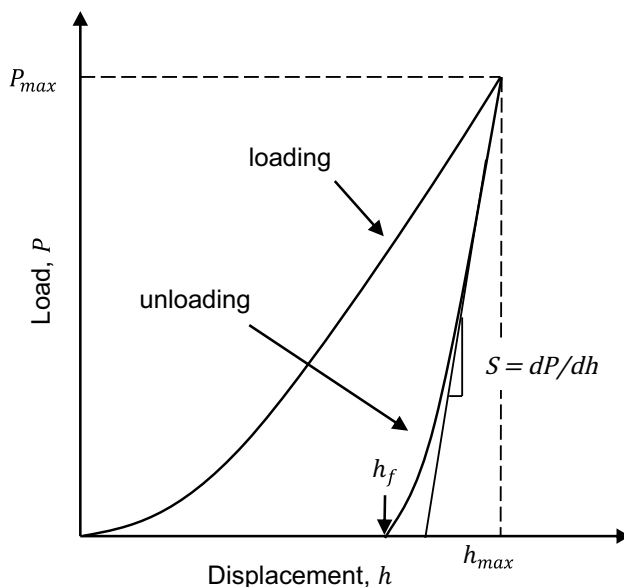
Fig. 1 Schematic illustration of the load–displacement curve. h_c, the contact depth; h_{max}, the maximum indentation depth; h_f, the residual depth; and S, the slope of the unloading curve (modified from Oliver and Pharr (2004))

Compared with conventional EDS, the AMICS is able to identify mineral phases automatically with a resolution of 1.0 μm. The samples prepared in Sect. 2.1 were used for AMICS analysis in an SEM (Crossbeam 540, ZEISS) equipped with a Bruker XFlash detector operating at 20 kV.

2.2 Real-Time Nanoindentation Tests Under the Heating–Cooling Cycle

Due to the high resolution and accuracy of nanoindentation in measuring properties at nanometer scale (Pethicai et al. 1983; Fröhlich et al. 1977; Newey et al. 1982; Liu et al. 2016), sample-conserving ability (Shukla et al. 2013), and non-destructive quality (Fischer-Cripps and Nicholson 2004), it was used to characterize the micromechanical properties of the minerals in this study. This section briefly introduces nanoindentation theory, followed by the experimental procedures of the real-time nanoindentation test in the heating–cooling cycle.

Theory of nanoindentation: The nanoindentation method, developed by Oliver and Pharr (1992) aims to measure the microscale mechanical properties of a material, such as elastic modulus and hardness. Specifically, load-displacement data were recorded during a loading-unloading cycle. The schematic representation of a typical nanoindentation test is shown in Fig. 1. The reduced modulus is calculated based on the slope of the unloading curve, which can be fitted by the following power-law relation:

$$P = \alpha(h - h_f)^m \tag{1}$$

where P is the indentation load; h is the indentation depth; h_f is the final depth after fully unloading; and m and α are power law fitting parameters, respectively. By taking the derivative of Eq. 1 at maximum depth h_{max}, the contact stiffness S is derived:

$$S = \frac{dP}{dh}\Big|_{h=h_{max}} = \alpha(h_{max} - h_f)^{m-1} \tag{2}$$

According to Hertz's contact theory (Hertz 1881), the reduced modulus E_r, corresponding to the combined mechanical properties of the indenter and specimen, is given by:

$$\frac{1}{E_r} = \frac{1 - \nu^2}{E} + \frac{1 - \nu_i^2}{E_i} \tag{3}$$

where E and ν is the elastic modulus and Poisson's ratio of the specimen, respectively; and E_i and ν_i is the elastic modulus and Poisson's ratio of the indenter tip, respectively.

Reduced modulus E_r can be read as follows:

$$E_r = \frac{\sqrt{\pi} S}{2\sqrt{A}} \tag{4}$$

where A is the projected contact area.

The contact area A is assumed as the function of contact depth h_c, known as the shape function or the area function, which is given by:

$$A = C_0 h_c^{\,2} + C_1 h_c + C_2 h_c^{1/2} + C_3 h_c^{1/4} \\ + C_4 h_c^{1/8} + ... + C_8 h_c^{1/128} \tag{5}$$

where $C_i (i = 0, 1, 2, ..., 8)$ are fitting constants. For a perfect Berkovich indenter, the shape function can be approximated by:

$$A = 24.5 h_c^{\,2} \tag{6}$$

where the contact depth h_c is given by:

$$h_c = h_{max} - \varepsilon \frac{P_{max}}{S} \tag{7}$$

where ε is the geometric correction factor, equal to 0.75 for Berkovich indenter; and P_{max} is the maximum load. Subsequently, the hardness H can be evaluated by the following equation:

$$H = \frac{P_{max}}{A} \tag{8}$$

Experimental procedure: The nanoindentation tests were conducted using a Hysitron TI950 Triboindenter equipped with a heating stage. A Berkovich diamond tip indenter with a half angle of 65.27 ° intended for high temperature (TI-0271, Bruker) was used. The indenter's Young's modulus E_r is equal to 1140 GPa, and Poisson's ratio v is equal to 0.07. The sample
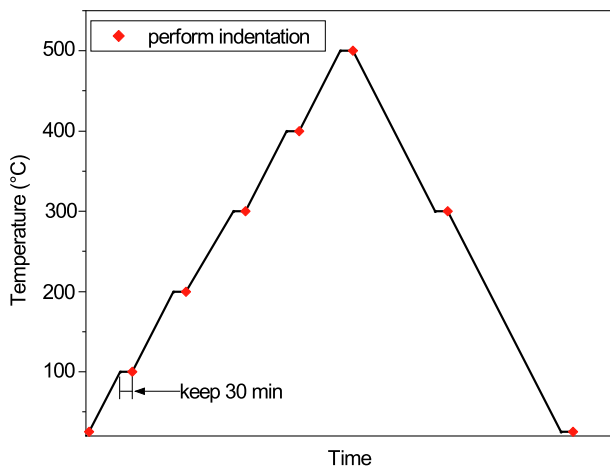
Fig. 2 Flow chart of nanoindentation tests during a heating–cooling cycle
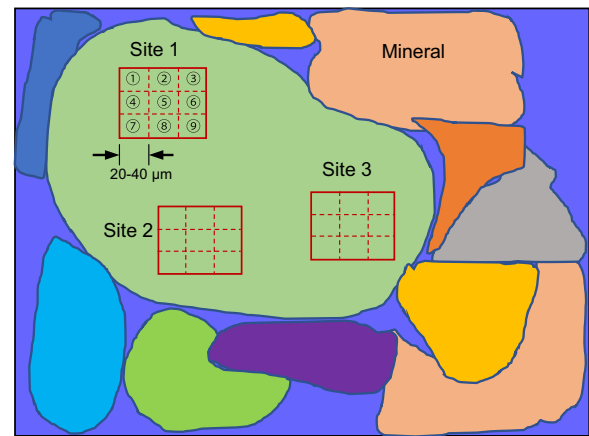
Fig. 3 Schematic diagram presenting indentation locations. Three sites were selected for nanoindentation tests within individual mineral grains. The grids labeled by circled numbers indicate areas of nanoindentation tests for different target temperatures

was heated from room temperature (RT) to a maximum temperature of 500 °C using the heating stage. Subsequently, the sample was cooled to RT naturally. During the heating and cooling processes, the nanoindentation tests were carried out at RT, 100 °C, 200 °C, 300 °C, 400 °C, and 500 °C, respectively. The flow chart of the nanoindentation test under the heating–cooling cycle is presented in Fig. 2. The following are the detailed experimental steps:

(a) Select indented area. Indentation areas absent of obvious defects, such as cracks, were selected using SEM (Quatrro S, Thermofisher) operated at 15 kV in low vacuum conditions. The constituent minerals were distinguished by EDS operated at 15 kV (EDS, MAX100, Oxford). In addition, the AMICS system (Sect. 2.1) aided in identifying the constituents. After transferring the sample to the Triboindenter, the selected areas by SEM were relocated with the assistance of an optical microscope. A squared image of surface topology with a scanning size ranging from $(20 \times 20)\ \mu m^2$ to $(40 \times 40)\ \mu m^2$ was then obtained by scanning probe microscope (SPM) to determine the exact location for indentation. Due to fabric heterogeneity of minerals and surface roughness variation, at least three sites were chosen to perform nanoindentation within each mineral grain. Each site was indented 5-6 times within a scanning area via SPM to ensure consistency and reliability of the measurement. Fig. 3 schematically shows the indentation location.

(b) Heat the sample to the target temperature. The heating rate was set to 5 °C/min to avoid thermal shock. The sample was kept at the target temperature for 30 min for thermal equilibrium.

(c) Heat the indenter tip to the target temperature. The indenter tip was touched to the sample surface and held for 3 min to ensure thermal stability between the indenter tip and sample.

(d) Perform nanoindentation. Nanoindentation tests were carried out in load-control mode with a maximum force of 3000 μN. The loading rate was set to 300 μN s^{-1}. The indenter was held for 2 s at the maximum load to eliminate the creep effect, and was then unloaded at a rate of -300 μN s^{-1}.

(e) Select a new indentation location near the previous ones. As Fig. 3 shows, the new location is selected next to the previous ones at each site.

(f) Repeat all of the previous steps until a heating–cooling cycle was completed.

## 2.3 Morphology Investigation Under the Heating–Cooling Cycle

After the nanoindentation tests, the morphology of the sample was examined under an optical microscope (LV100N, Nikon) and an ESEM (Quattro S, ThermoFisher); however, real-time changes in morphology could not be captured in this way. Consequently, the ESEM equipped with a hot stage (Quattro S, ThermoFisher) was utilized to observe the evolution of surface morphology during the heating and cooling process. Samples with the size of $\phi 3.5 \times 1$ mm were prepared for this investigation to adapt the hot stage's holder. The same procedure of surface polishing as in Sect. 2.1 was applied to reduce sample roughness. A (1.5×1.5) mm^2 region selected in the center of the sample was observed during the heating and cooling processes. The sample was heated to a maximum temperature of 500 °C from RT with a heating rate of 5 °C/min, and then cooled down to RT naturally. In the meantime, samples were held at the following temperatures to collect SEM micrographs of the selected area: 100 °C, 250 °C, 350 °C, and 500 °C.

2.4 Mineral Structure Characterization and Thermal Decomposition Analysis

The variation of the crystal structure (i.e., the ordered arrangement of atoms, ions, or molecules) can affect its mechanical properties (Duffy and Vaughan 1988). Su et al. (2021) concluded that the elastic moduli of crystals decreased as their thermal expansion coefficients increased, resulting from the mechanism of weakening of intermolecular interactions. Therefore, real-time high-temperature XRD tests were performed to examine changes in the mineral structure. Moreover, the thermal decomposition of minerals

Table 2 Mineral composition of the sample

Minerals	Mass (%)	Area (%)
Plagioclase	52.90	55.36
Amphibole	17.43	14.81
Biotite	10.68	10.28
Quartz	8.16	8.89
Alkali feldspar	1.92	2.16
Others	8.91	8.50
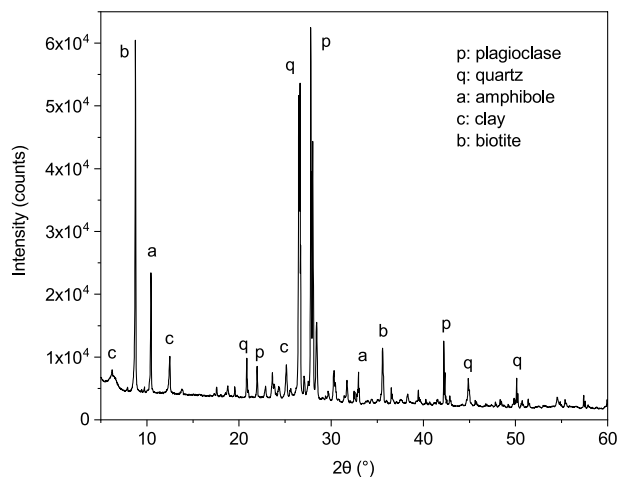
Fig. 4 XRD pattern of the sample. Main characteristic peaks of each mineral are indicated

could alter their structure, such as dehydroxylation of phlogopites (Tutti and Lazor 2000) and decomposition of carbonates (Kobchenko et al. 2011). As a consequence, thermal composition analysis was carried out based on combined thermogravimetric analysis and Fourier's transform infrared spectroscopy (TG-FTIR).

High-temperature real-time structural characterization of minerals: A high-temperature XRD experiment was implemented to characterize in real time the microstructure of mineral crystals. Samples with a size of $\phi 15 \times 1.5$ mm were prepared for the XRD tests, conducted on an X-ray diffractometer (Smartlab 9kW, Rigaku) equipped with a heating stage (HTK 1200, Anton Parr). The operating voltage and current used were equal to 40 kV and 30 mA, respectively, with a copper anode. The scanning angle 2θ ranged from 15° to 60°, with a scanning speed of 5° min^{-1}, and an interval of 0.02°. The sample was heated from RT to the maximum temperature of 800 °C at a rate of 10 °C min^{-1}, and then cooled down to RT naturally. During the heating, the XRD patterns were collected at the following temperatures: 100 °C, 150 °C, 200 °C, 250 °C, 300 °C, 350 °C, 400 °C, 500 °C, 550 °C, 600 °C, 700 °C, 750 °C, and 800 °C.

TG-FTIR tests: TG and FTIR were combined to investigate thermal decomposition, including mass changes and mineral reactions during heating (TG-IR-GC/MS system, PerKinElmer). A powdered sample weighing 50 mg with the same size as that in the powdered XRD experiment (see Sect. 2.1) was used for TG analysis under temperatures increasing from RT to 1000 °C in N_2 atmosphere. FTIR was also used to simultaneously detect decomposition products, such as water and carbon dioxide.
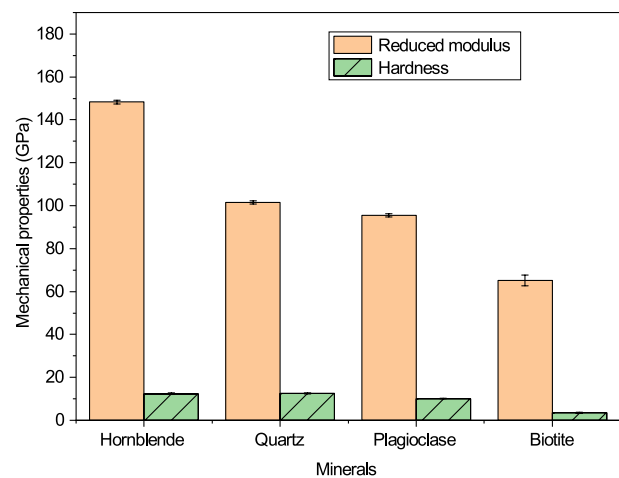
3 Results

First, the mineral composition of the sample is presented. Second, the nanoindentation test results are given, including the micromechanical properties at RT and during the heating–cooling cycle. This is followed by morphology characterization results of the sample surface after the heating–cooling treatment and those acquired in real time under heating–cooling conditions. Finally, changes in mineral structure during high temperatures and the results of thermal decomposition analysis are provided.

3.1 Mineral Composition

The XRD pattern is presented in Fig. 4, showing that the sample examined mainly consists of plagioclase, quartz, amphibole, biotite, augite, and clay minerals. The percentage of minerals obtained by the AMICS system is listed in Table 2, which shows that plagioclase, amphibole, biotite, quartz, and alkali feldspar comprise more than 90 wt% of the whole mineral composition. In addition, Fig. 5 illustrates a representative BSE image and its corresponding mapping of mineral distribution recovered from the AMICS system. Fig. 5 shows that defects, such as pores, micro-cracks, and inclusions, are contained within the mineral grains. The indentation location should remain non-proximal to those defects.
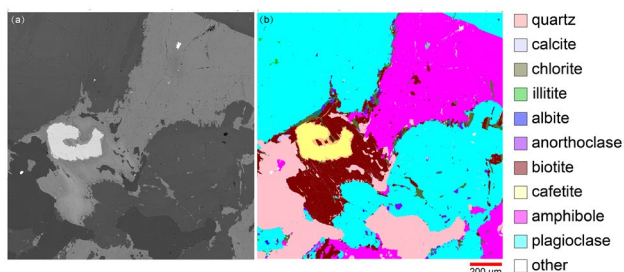
Fig. 5 **a** A representative BSE image; and **b** mineral mapping of **a** obtained by the AMICS system


Fig. 6 Reduced modulus and hardness of main constituent minerals at room temperature

3.2 Mechanical Characterization of Minerals

According to the mineral composition results (refer to Sect. 3.1), four main minerals were investigated in the nanoindentation tests, i.e., quartz, plagioclase, amphibole, and biotite.

Mechanical properties of minerals at RT: The reduced modulus and hardness of main constituent minerals calculated based on the Oliver-Pharr method are shown in Fig. 6. The results revealed that both the reduced modulus (approximately 65 GPa) and hardness (< 3.5 GPa) of
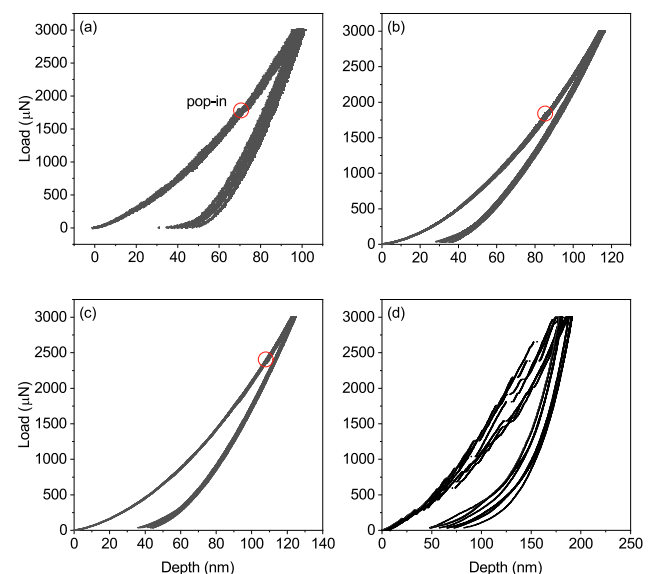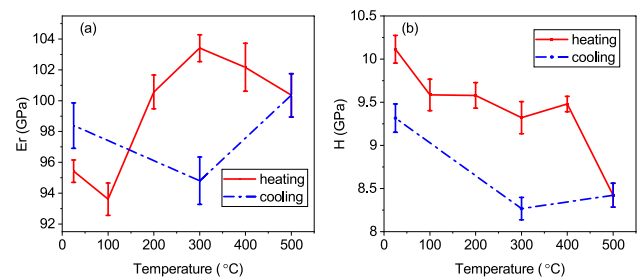

Fig. 7 Load-depth curve for different minerals at RT. **a** Amphibole (7 testing curves); **b** quartz (16 testing curves); **c** plagioclase (10 testing curves); and **d** biotite (7 testing curves). The red circles indicate that "pop-in" occurred during nanoindentation

4410 C. Mo et al.

biotite are the lowest, while these values are the highest for amphibole. Furthermore, the pattern of load-depth curves of minerals were different from each other (Fig. 7). Specifically, biotite has the highest maximum depth (approximately 180 nm) and residual depth (approximately 60 nm), which explains why it has the lowest hardness and distinct indentation after entirely unloading. The maximum indentation depth of amphibole was less than 100 nm, which is the lowest among all of the minerals investigated, corresponding to its high hardness. In addition, the unloading curve slope of biotite was the steepest compared with other minerals, which is consistent with its highest reduced modulus. It is worth noting that apparent "pop-in" occurred in biotite at the loading portion [Fig. 7d], resulting from kink band creations and layer delamination (Zhang et al. 2013). Nevertheless, the unremarkable "pop-in" was found in amphibole, quartz, and plagioclase [Fig. 7a, b, and c], which may result from plastic deformation (Pathak and Kalidindi 2015) with bursts of dislocation nucleation and motion (Shim et al. 2008).

Mechanical properties of minerals during the heating–cooling cycle: With the assistance of the Triboindenter equipped with a hot stage, the reduced modulus and hardness of various minerals were obtained during the heating–cooling cycle. The reduced modulus and hardness of quartz exhibited general trends of decrease during the heating process. As the temperature increased from RT to 100 °C, the reduced modulus increased slightly. The reduced modulus decreased negligibly as temperature increased from 100 to 400 °C. The hardness of quartz exhibited a similar trend to its reduced modulus during heating. Interestingly, a significant reduction of reduced modulus (decreased by 11.2%) and hardness (decreased by 18.8%) was found when the temperature increased from 400 to 500 °C. Compared with RT, the reduced modulus and hardness of quartz at the temperature of 500 °C decreased by 12.6% and 21.6%, respectively. When the sample was cooled from 500 °C to RT, both the reduced modulus and hardness of quartz
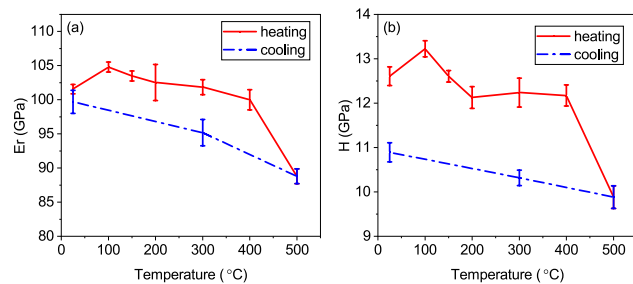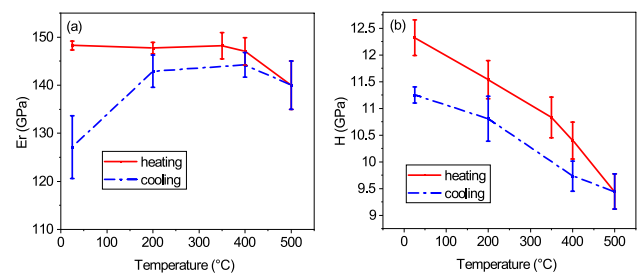

Fig. 9 Reduced modulus and hardness of plagioclase change with temperature during the heating–cooling cycle. **a** Reduced modulus as a function of temperature; and **b** hardness as a function of temperature
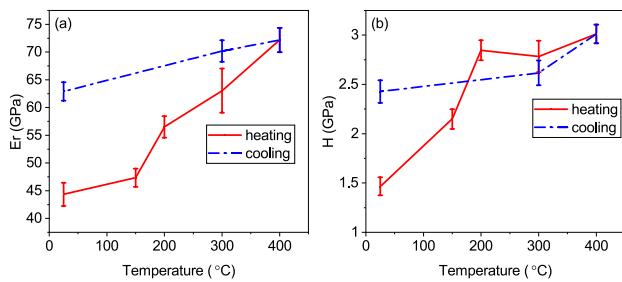
increased linearly, but lowered compared to those at corresponding heating temperatures. Compared to the heating temperature of 300 °C, the reduced modulus and hardness of quartz decreased by 6.5% and 15.7%, respectively, when the sample was cooled down to 300 °C. After a cycle of heating–cooling, the reduced modulus of quartz almost recovered completely (decreased by 1.8%) compared to that at the initial RT. However, the hardness of quartz dropped by 13.6% after the heating–cooling treatment.

Concerning plagioclase, its reduced modulus increased from 95.43 GPa at RT to 103.41 GPa at 300 °C (increased by 8.37%) [Fig. 9a], except for a slight decline at 100 °C. As the temperature increased from 300 °C to 500 °C, the reduced modulus fell marginally (dropped by 2.95%). It should be noted that all of the reduced moduli of plagioclase at the heating process were higher than those at RT, except for 100 °C. At the cooling stage, there was no significant variation of reduced modulus for plagioclase. The results showed a reduction of 5.5% for reduced modulus as temperature dropped from 500 °C to 300 °C. The reduced modulus of plagioclase increased by 3.8% when the temperature recovered from 300 °C to RT. The hardness of plagioclase exhibited a hysteric pattern during the heating–cooling cycle [Fig. 9b], similar to that of quartz [Fig. 8b]. Hardness presented a general trend of reduction

Fig. 8 Reduced modulus and hardness of quartz change with temperature during the heating–cooling cycle. **a** Reduced modulus as a function of temperature; and **b** hardness as a function of temperature

Fig. 10 Reduced modulus and hardness of amphibole change with temperature during the heating–cooling cycle. **a** Reduced modulus as a function of temperature; and **b** hardness as a function of temperature

Fig. 11 Reduced modulus and hardness of biotite change with temperature during the heating–cooling cycle. **a** Reduced modulus as a function of temperature; and **b** hardness as a function of temperature

during heating and increased during the cooling process. The values during the cooling, however, lowered compared to those at the corresponding heating temperature. Hardness declined by 5.2% as the temperature increased from RT to 100 °C, and remained almost constant until the temperature reached 400 °C. Hardness dropped by 7.4% at 500 °C, compared with that at 400 °C. Subsequently, a trend analogous to the reduced modulus of plagioclase was observed during the cooling process. An increase of 10.6% was found for the hardness of plagioclase after cooling down to RT compared with that at 500 °C. After the heating–cooling treatment, the hardness of plagioclase decreased by 7.9%.

For amphibole, its reduced modulus and hardness during the heating–cooling cycle is shown in Fig. 10. During heating, the reduced modulus of amphibole did not show a significant change until 350 °C, and decreased by 5.6,% at 500 °C compared with that at RT [Fig. 10a]. At the subsequent cooling stage, the reduced modulus increased until 400 °C, and then declined. The reduced modulus at 400 °C and 200 °C were slightly lower than the corresponding values during heating (i.e., 1.9% and 3.2% lower, respectively). It is evident in Fig. 10a that a sharp reduction of reduced modulus exists (decreased by 14.3%) when the temperature returned to RT compared with that without thermal treatment. Meanwhile, the hardness of amphibole decreased with temperature and increased during cooling [Fig. 10b]. A 23.4% decline of hardness for amphibole was found at the heating temperature of 500 °C compared with that without thermal treatment. Similar to quartz and plagioclase, the hardness of amphibole during cooling lowered compared to the corresponding ones during heating (i.e., when cooling to 400 °C, 200 °C and RT, hardness decreased by 6.4%, 6.3%, and 8.7%, respectively).

The variation of mechanical properties of biotite with temperature is displayed in Fig. 11. A hysteresis pattern was also identified for the reduced modulus of biotite [Fig. 11a]. However, the trend of reduced modulus for

biotite during heating and cooling were the opposite to that of quartz [Fig. 8a], i.e., its reduced modulus increased significantly with temperature and then decreased linearly during the cooling process. Compared with RT, an increase of 62.3% was found for the reduced modulus when temperature increased to 500 °C. Meanwhile, a reduction of 12.9% was discovered as temperature cooled from 450 °C to RT. Despite this, the reduced modulus of biotite after heating–cooling treatment was still higher than that at initial RT (increased by 41.2%). The hardness of biotite also exhibited a noticeable growth trend during the heating process, especially from RT to 200 °C [Fig. 11b]. At the cooling stage, hardness decreased as temperature declined. Hardness decreased by 19.6% after cooling down to RT in comparison with that at 500 °C. Similarly, the hardness of biotite increased greatly after the heating–cooling treatment (increased by 65.3%).

3.3 Characterization of Surface Morphology During Heating and Cooling

The morphology of the sample after the nanoindentation test is presented. In addition, real-time morphology characterization results of the sample surface based on SEM under heating and cooling conditions are given.

Changes in morphology after heating–cooling treatment: Optical micrographs of the samples before and after treatment are presented in Fig. 12. SEM micrographs and EDS mapping diagrams are also shown in Fig. 13. Both types of graphs show that thermally-induced micro-cracks were generated after the heating–cooling treatment. The inter-granular cracks were abundant, including types of plagioclase-plagioclase [Fig. 12b], biotite-plagioclase [Fig. 12f], biotite-quartz [Fig. 12h], and quartz-plagioclase [Fig. 13b]. In contrast to the inter-granular cracks, the number of trans-granular ones was less. It is worth noting that trans-granular microcracks were found to occur more commonly within the biotite grains [Figs. 12h and 13c]. Due to the lamellar structure of biotite, the thermal cracks tended to initiate between its inter-layers [Fig. 12b, c, and f]. Furthermore, intra-granular thermal cracks can be observed, such as cracks within quartz grains [Figs. 12d; 13b] and plagioclase grains [Figs. 12b and h; 13b].

Real-time SEM observation during heating and cooling: Real-time SEM observation during the heating and cooling processes was performed to further determine thermal influence on the samples [Fig. 14]. During the heating process [Fig. 14a], the thermally-induced cracks initiated at low temperatures (e.g., < 250 °C). As temperatures increased, these cracks propagated and began to join together. At higher temperatures (e.g., 500 °C), through-cracks ultimately formed and some cracks bifurcated. In addition, thermally-induced cracks were found when the
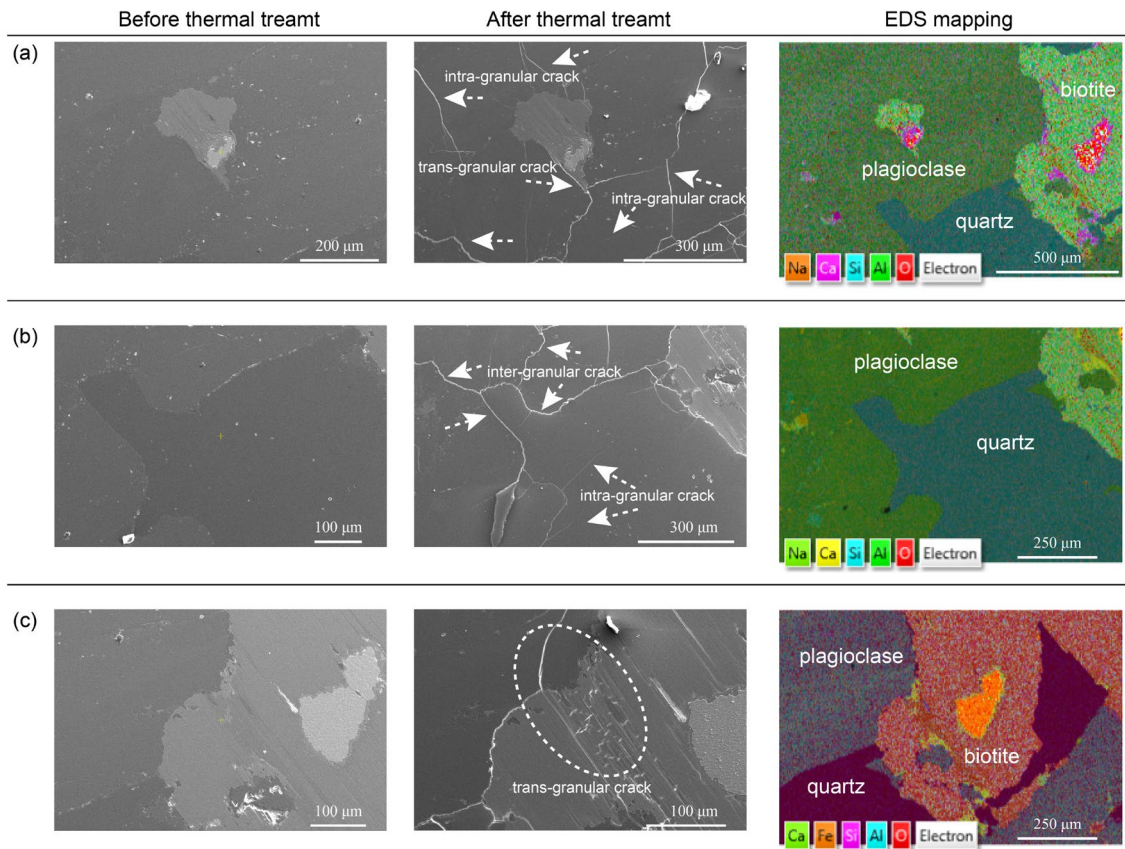
Fig. 12 Optical micrographs of the samples before thermal treatment [(**a**),(**c**),(**e**), and (**g**)] and after thermal treatment [(**b**), (**d**), (**f**), and (**h**)]

Before thermal treatment

After thermal treatment
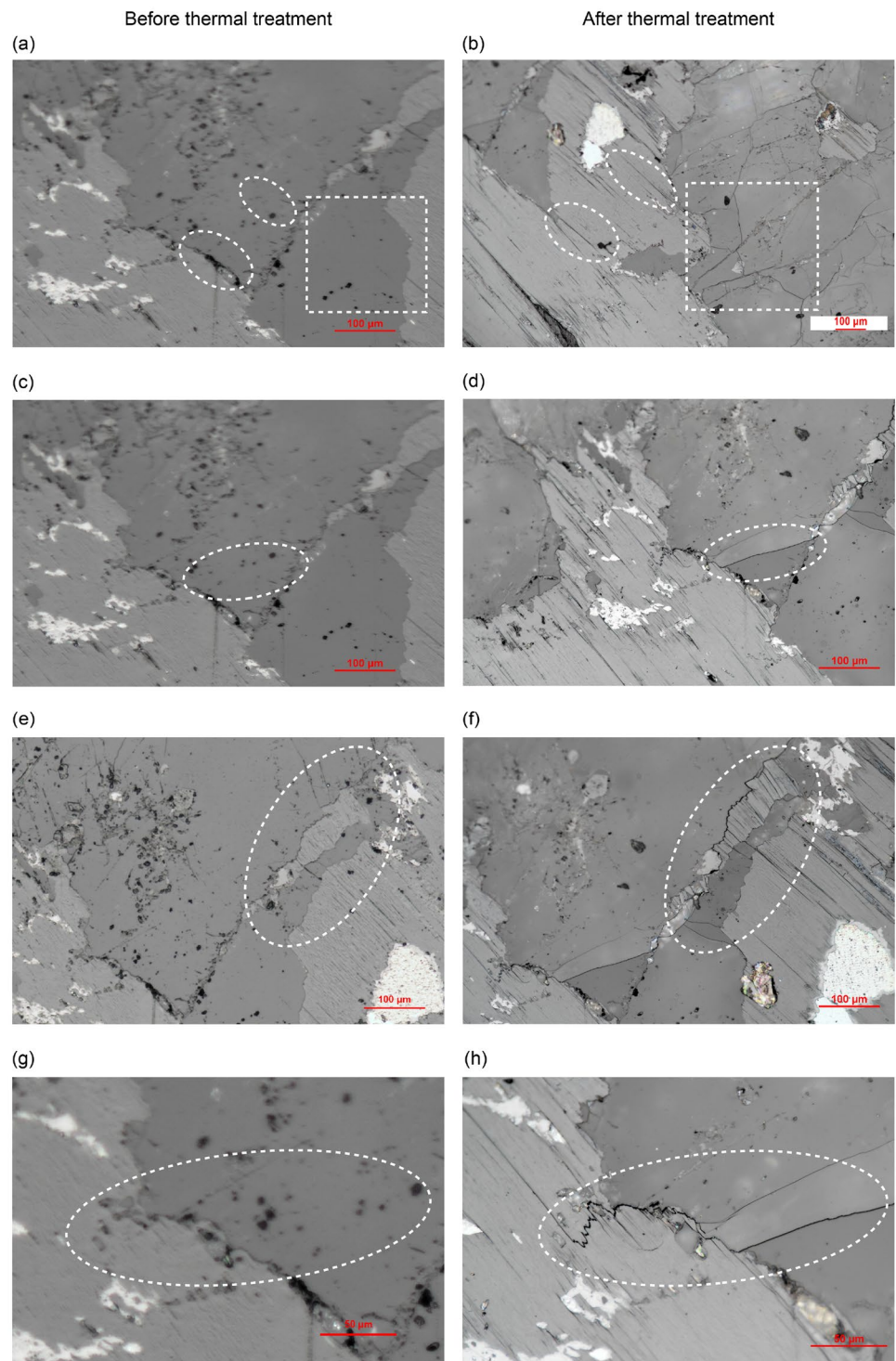
sample was subjected to cooling [Fig. 14b]. During the cooling process, however, some induced cracks generated at the heating stage were found to close with their apertures decreased (i.e, crack closure) [Fig. 14c].

3.4 Changes in Mineral Structure at High Temperatures and Thermal Decomposition

This section presents the results of high-temperature XRD, revealing the real-time structural alteration of minerals, and

Fig. 13 SEM micrographs of the samples before thermal treatment and after thermal treatment. Three typical sites are selected: **a** site 1; **b** site 2; and **c** site 3
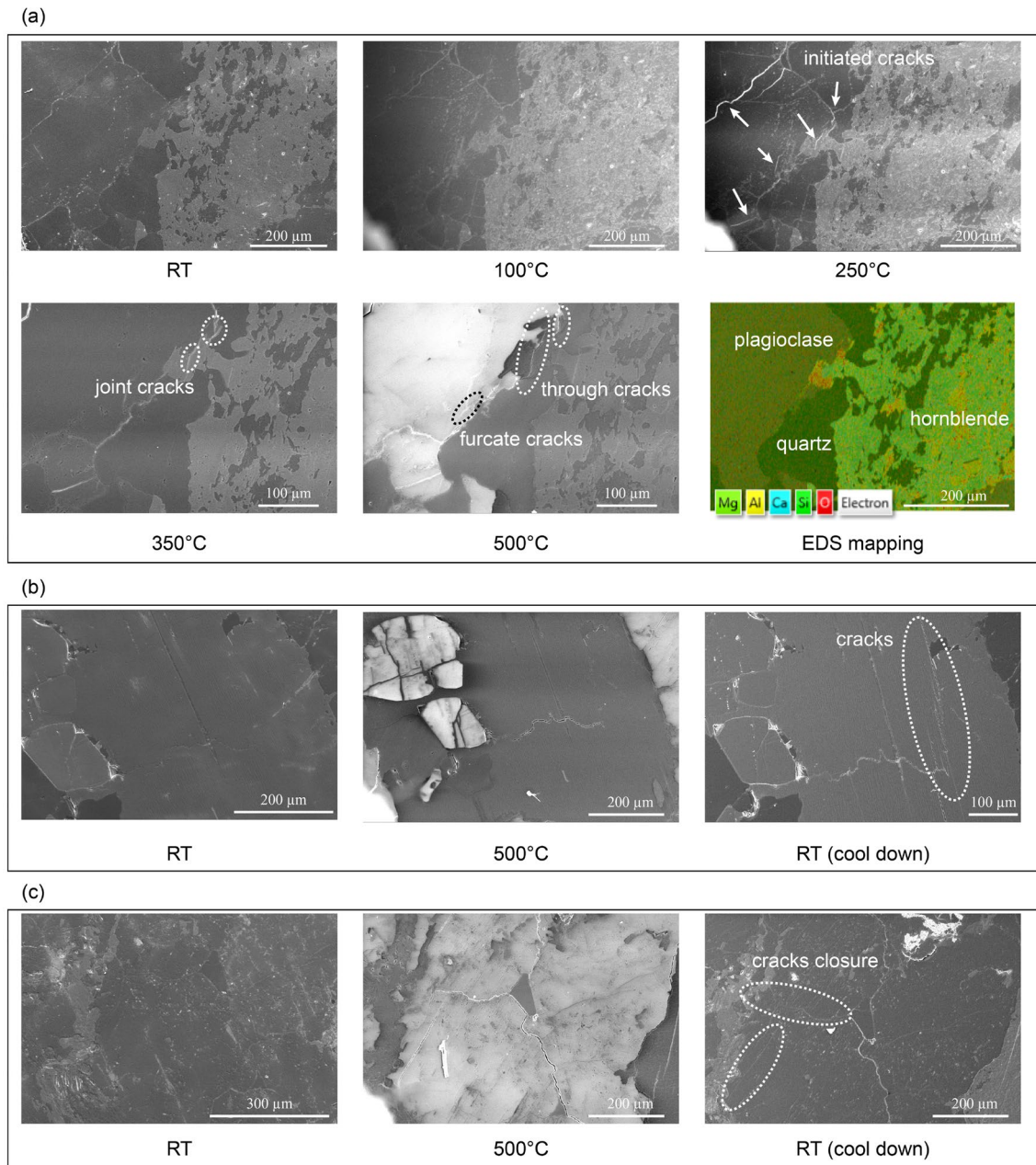
TG-FTIR analysis, indicating the decomposition of minerals at high temperatures.

Structural changes of mineral crystals at high temperatures: According to Bragg's law, the spacing of the lattice plane can be derived from the diffraction angle in an XRD pattern. The crystal plane (100) and (101) of quartz showing the highest diffraction intensity were investigated (Fig. 16). Below 600 °C, the spacing of plane (100) and (101) increased exponentially with temperature. A turning point existed for both plane (100) and plane (101) at 600 °C [Fig. 16a and b]. Afterward, the spacing exhibited a slight decrease. These changes of plane spacing were probably due to the $\alpha - \beta$ transformation of quartz occurring at 573 °C. The full width at half maximum (FWHM) of the XRD pattern can indicate the variation in microstructure and stress or strain accumulation, such as grain distortion, dislocation density, and residual stress (Noyan and Cohen 2013). The variation of FWHM with temperature for plane (100) and plane (101) is shown in Fig. 16c and d, respectively. A slight decrease was observed for the FWHM of plane (100). The FWHM of plane (101) exhibited a decrease at first (from RT to 200 °C), followed by an increase (from 200 °C to 600 °C), and then decreased (above 600 °C).

Meanwhile, the two representative crystal planes of plagioclase, i.e., plane ($\bar{2}$01) and plane ($\bar{2}$02), were examined (Fig. 17). The lattice spacing of these two planes generally decreased with temperature [Fig. 17a and c]. Moreover, the FWHM of plane ($\bar{2}$01) reduced as temperature increased. Nevertheless, the FWHM of plane ($\bar{2}$02) increased at first (from RT to 100 °C), and then fell (from 100 °C to 300 °C), before marginally increasing.

For amphibole, the variation of lattice spacing and FWHM with temperature is shown in Fig. 15. Below 500 °C, lattice spacing increased with temperature [Fig. 15a]. Afterward, it dropped as temperature increased, especially at 800 °C. The FWHM of plane (301) hardly changed with temperature before the temperature reached 500 °C [Fig. 15b]. However, a distinct increase was identified at 700 °C.

The changes in biotite structure with temperature are illustrated in Fig. 18. The two selected planes, (001) and (002), generally increased with temperature. The spacing of plane (001) increased when the temperature was below 300 °C, and then decreased slightly (Fig. 18). The spacing of plane (002) showed a steady increase during the heating process [Fig. 18b]. The FWHM of plane (001) generally

(a)

RT

100°C

250°C

initiated cracks

350°C

joint cracks

500°C

through cracks

furcate cracks

EDS mapping

plagioclase

quartz

hornblende

Mg Al Ca Si O Electron 200 μm

(b)

RT

500°C

RT (cool down)

cracks

(c)


RT

500°C

RT (cool down)

cracks closure

Fig. 14 SEM micrographs of the samples during heating and cooling processes. During the heating process, cracks initiate, join, and form through ones at 250 °C, 350 °C, and 500 °C, respectively (**a**); during the cooling process, new cracks generate (**b**) and cracks induced during the heating process can be closed (**c**)

increased as temperature increased, showing a fluctuation around (300 to 400)°C [Fig. 18c], similar to that of plane (002) [Fig. 18d].

Mass loss and mineral reaction at high temperatures: The results of TG-FTIR are shown in Fig. 19. It is found that the mass decreased by 0.84% after heating to 1000 °C [Fig. 19a]. Below approximately 560 °C, the mass reduced marginally (< 30% of total mass loss). The reason for this

mass loss can be attributed to the decomposition of water and carbon dioxide detected by the FTIR [Fig. 19b]. The results of FTIR revealed that the spectrum intensity of water slowly increased as temperature increased from RT to 560 °C, and peaked at 630 °C. Furthermore, carbon dioxide mainly decomposed at approximately 720 °C.
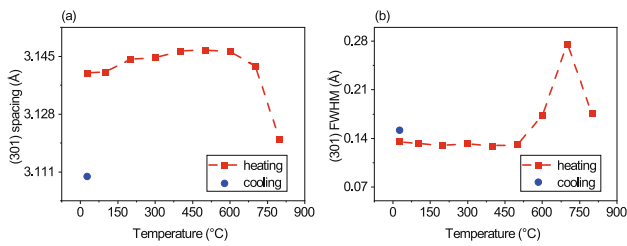
Fig. 15 The changes in the (301) lattice plane of amphibole with temperature. **a** spacing of lattice plane (301) varies with temperature; and **b** FWHM of lattice plane (301) varies with temperature
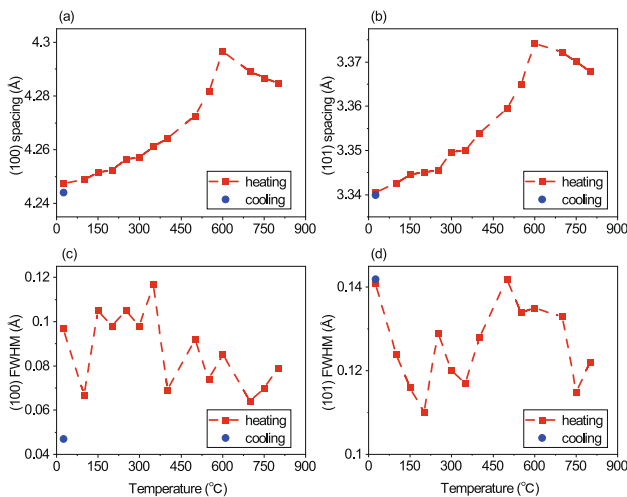

Fig. 16 Structural variations in plane (100) and plane (101) of quartz with temperature. **a** and **b**, variations of spacing of plane (100) and (101) with temperature, respectively; and **c** and **d** variations of FWHM of plane (100) and (101) with temperature, respectively
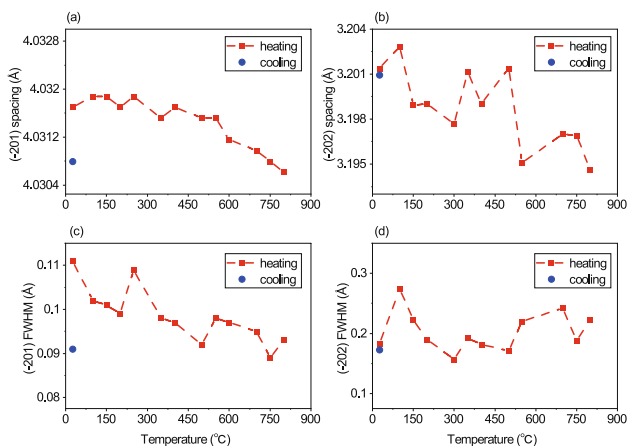
Fig. 17 Structural variations of plane ($\bar{2}$01) and plane ($\bar{2}$02) in plagioclase with temperatures. **a** and **b** variations of spacing of plane ($\bar{2}$01) and ($\bar{2}$02) with temperature, respectively; and **c** and **d** variations of FWHM of plane ($\bar{2}$01) and ($\bar{2}$02) with temperature, respectively
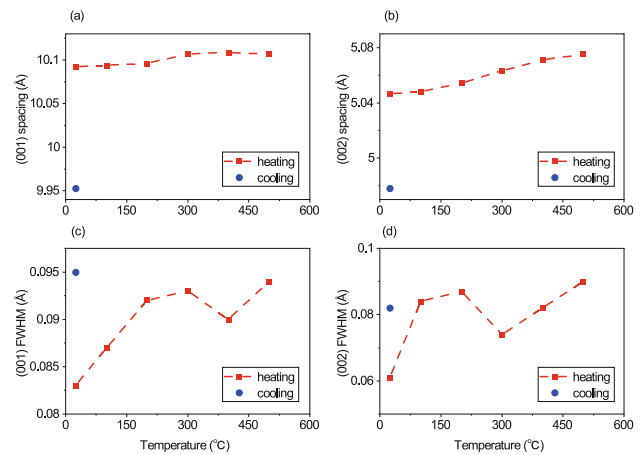
Fig. 18 Structural variations in plane (001) and plane (002) of biotite with temperature. **a** and **b** variations of spacing of plane (001) and (002) with temperature, respectively; and **c** and **d** variations of FWHM of plane (001) and (002) with temperature, respectively
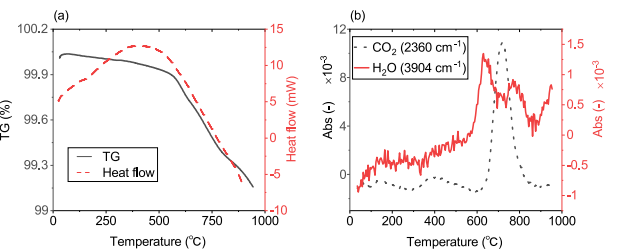
Fig. 19 Results of the combined thermogravimetric analysis and Fourier-transform infrared spectroscopy (TG-FTIR). **a** Variation of mass loss and heat flow with temperature; and **b** variation of FTIR intensity of water and carbon dioxide with temperature. The characteristic absorption spectrum of $3904\,cm^{-1}$ and $2360\,cm^{-1}$ was selected for water and carbon dioxide, respectively

4 Discussion

The results of the nanoindentation test at RT in this study are compared with those in the literature to confirm data reliability. The underlying mechanisms of temperature effect on the mechanical properties of minerals are then analyzed, including the heating effect and cooling effect. Implications of the mechanical properties of minerals for the macroscale mechanical properties of rocks are also discussed.

4.1 Comparison with Reported Mechanical Properties of Minerals

The comparison of the Young's moduli E and hardness of various minerals are listed in Table 3. From Eq. 3, Young's modulus of minerals can be obtained if Poisson's ratios are given. The Poisson's ratio of quartz, plagioclase,

Table 3 Comparison of measured Young's modulus E and hardness H of various minerals with those from the literature

Reference	Quartz		Feldspar		Amphibole		Mica	
	E (GPa)	H (GPa)	E (GPa)	H (GPa)	E (GPa)	H (GPa)	E (GPa)	H (GPa)
Maruvanchery and Kim (2020)	~ 105.3	11.6	77.6	8.4	–	–	–	–
Mavko et al. (2020)	94–96	–	69.0[a]	–	–	–	33–103	–
Zhu et al. (2007)	100–110	12–14	62–88[b]	5–10[b]	–	–	59.2 ± 8.1[c]	3.3 ± 0.6[c]
Lanin et al. (2021)	89.6 ± 19.7	–	–	–	–	–	30.0[d] , 95.4[e]	–
Vyzhva et al. (2014)	–	–	–	–	–	–	52–59	–
Zhang et al. (2010)	–	–	–	–	–	–	37.0 ± 0.9	–
Zhang et al. (2013)	–	–	–	–	–	–	–	3.3
Brown and Abramson (2016)	–	–	–	–	141.8–157.1	–	–	–
Zhao et al. (2019)	87.2	–	66.8	–	–	–	–	–
This work	110.9	12.6	94.8	10.1	155.0	12.3	44.4	1.5

[a] Albite

[b] Mixture of albite and orthoclase feldspar

[c] Muscovite containing Mg/Fe

[d] Loading normal to the layer plane

[e] Loading parallel to the layer plane
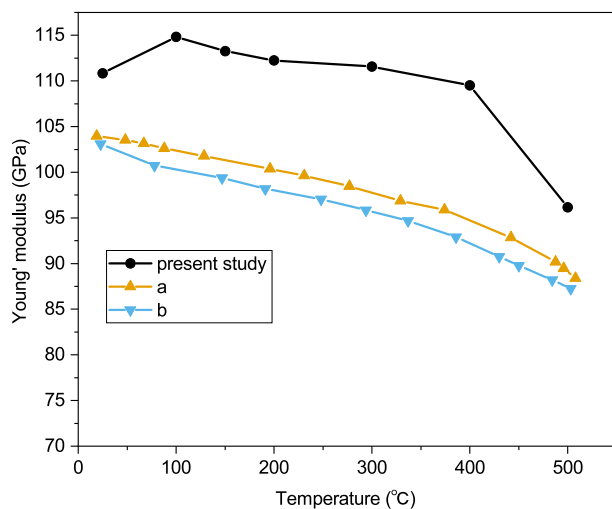
Fig. 20 Comparison of Young's moduli of quartz during heating with those in the literature. Dataset a from Ohno et al. (2006) and b from Lakshtanov et al. (2007)

amphibole, and biotite was assumed to be 0.07, 0.3, 0.3, and 0.3, respectively (Mavko et al. 2020). The Young's modulus and hardness of quartz were adequately within the reported data ranges. In addition, the Young's modulus of amphibole in this study was well within the range of the reported data from the literature. For feldspar, our test values were comparable with the results specified in the literature. In contrast, the published results of biotite were more varied. Due to the complex, layered structure of mica, its mechanical properties exhibit anisotropy when loading from different directions, such as loading parallel or normal to the layer plane. The obtained results for biotite may differ as the result of chemical impurities, cleavage, crystal defect and scale dependence, even when measured from the same layer plane (Lanin et al. 2021). The average Young's modulus of biotite is 63.0 GPa, between 30.0 and 94.5 GPa obtained by loading normal to and parallel to its layer planes, respectively (Lanin et al. 2021). We speculate that the loading direction in nanoindentation tests was inclined to the layer plane. In aggregate, our test results are comparable with those in the literature, confirming our data quality.

4.2 Mechanism of Thermal Effect on Micromechanical Properties

The experimental results indicated that the mechanical properties of different minerals have various responses to temperature. The reduced modulus and hardness of quartz generally decreased with temperature during heating and increased during subsequent cooling (Fig. 8). For plagioclase, the hardness exhibited the same variation trend as quartz during the heating and cooling processes. In contrast, its reduced modulus showed an increase, followed by a decrease, during heating and showed no significant variation during cooling (Fig. 9). In terms of biotite, its mechanical properties significantly improved as temperature increased, and then reduced as temperature decreased (Fig. 11). In this section, the underlying mechanism of these variations is discussed in terms of two aspects, i.e., the effects of heating and cooling.

Heating effect: Compared to the literature, the changes in Young's moduli of quartz during heating in the present study are consistent (Fig. 20). Our measured values of Young's moduli were generally higher and more varied than those reported in the literature. This difference could be ascribed to the following reasons: difference in test samples and experimental technique. First, the test samples used in the literature were single crystals of quartz that hardly contained impurities and inclusions (Lakshtanov et al. 2007). However, the quartz within samples cut from natural rock could include various defects and inclusions. Second, the characteristics of the ultrasonic or Brillouin method are markedly different from those of nanoindentation. Majumdar et al. (2008) suggested that nanoindentation provided an accurate evaluation of elastic modulus for homogenous materials. Instead, elastic modulus measured via the ultrasonic method can better characterize bulk material properties. For example, Young's moduli of bulk metallic glass measured by nanoindentation were approximately 31% greater than those obtained from ultrasonic methods, resulting from its non-homogeneous and anisotropic structure (Wu et al. 2019).

The α quartz transforms to β at approximately 573 °C, which leads to alteration of its mechanical behaviors (Lakshtanov et al. 2007; Ohno 1995; Ohno et al. 2006; Kimizuka et al. 2003). During this transition, Kimizuka et al. (2003) concluded that the relaxation of the internal strain among atoms contributed to reducing the macroscopic elasticity of quartz at high temperatures. Moreover, the atomic disorder of quartz can result in alteration of its crystallinity and expansion of unit-cell volume at high temperatures (Tucker et al. 2001), which produces the variation in FWHM and the increase in the spacing of lattice planes (Fig. 16).

Regarding plagioclase, its reduced modulus increased first, and then decreased at approximately 300 °C during heating [Fig. 9a]. In contrast to quartz, the spacing of lattice planes increased with temperature, and FWHM is apparently correlated with temperature (Fig. 17). The crystal structure of plagioclase was found to change at high temperature, such as the order-disorder of Al/Si (Winter et al. 1979; Zhang et al. 1996) and the inversion of triclinic-monoclinic symmetry for anorthoclase. During heating, the displacive phase transition of anorthoclase was observed at (200 to 300)°C due to the mechanism of structural water incorporation (Liu et al. 2018; Yang et al. 2016). The temperature of this transition is consistent with the turning point in Fig. 9a. The results of TG-FTIR tests (Fig. 19) indicated that the detected water was partially decomposed by plagioclase. A sudden dip of the FWHM for plane $\bar{2}02$ at 300 °C [Fig. 17d] further corroborated the phase transition occurrence. Therefore, we speculated that the alteration of crystal structure and water desorption controlled the reduced modulus of plagioclase during heating.
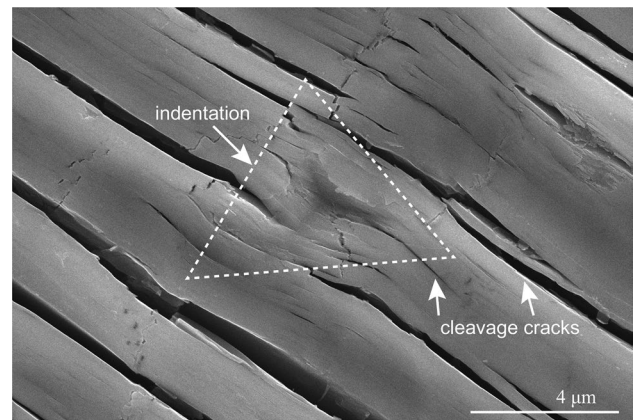

Fig. 21 A typical indentation within biotite. The length scale of indentation is several orders of magnitude larger than the spacing of open cleavage cracks

The reduced modulus and hardness of amphibole generally diminished during heating (Fig. 10), which can be explained by lattice spacing increase, as well [Fig. 15a]. Riecker and Rooney (1969) found that amphibole was weakened at 800 °C due to the dehydration reaction. This dehydration reaction consisted of the relatively apparent lattice spacing reduction at 800 °C (Fig. 15). Since the maximum heating temperature of 500 °C during the nanoindentation test was below the dehydration reaction temperature, 800 °C, the reduced modulus of amphibole did not show substantial degradation during heating. In contrast, hardness was more sensitive to high temperatures, decreasing almost linearly during heating.

Due to the layered structure, the mechanical properties of biotite showed different characteristics from quartz and plagioclase. The toughness of biotite measured in real time was enhanced during heating, increasing the macroscale mechanical strength of granites (Ma et al. 2020). The nanoindentation results of Fan et al. (2018) indicated that the elastic modulus and hardness of mica increased by 72% and 154%, respectively, after thermal treatment with a maximum temperature of 500 °C. These results agree with those in this study, to a certain extent, as the reduced modulus and hardness of biotite increased by 62,% and 65,%, respectively, after thermal treatments (Fig. 11). Although the spacing of lattice planes increased during heating (Fig. 18), the open cleavage cracks probably controlled the mechanical properties of biotite. The length scale of indentation within biotite were several orders of magnitude larger than the spacing of open cleavage cracks (Fig. 21). During heating, the loss of combined water and structural water by biotite probably led to shrinkage of the spacing along cleavages, and thus enhanced the mechanical properties (Fan et al. 2018).

Cooling effect: The mechanical properties of quartz increased during cooling. After the heating–cooling cycle

Fig. 22 Comparison of SEM micrograph of biotite before thermal treatment with that after thermal treatment. Three typical regions circled by ellipses are marked. **a** SEM micrograph before thermal treatment; and **b** SEM micrograph after thermal treatment
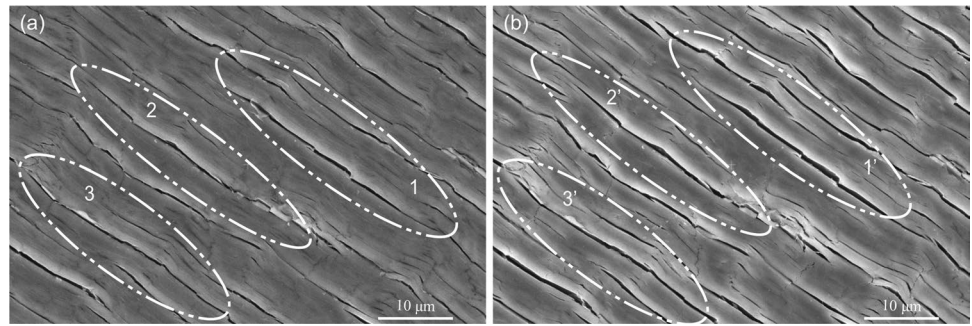
treatment, the reduction percentage for reduced modulus (decreased by 1.8%) and hardness (decreased by 13.6%) was comparable with that reported by Maruvanchery and Kim (2020), i.e., decreased by approximately 6% and < 3% for reduced modulus and hardness, respectively. In addition, the reduced modulus of plagioclase fluctuated at (95 to 101) GPa, and its hardness exhibited an evident increase during cooling. Maruvanchery and Kim (2020) found that the reduced modulus and hardness of plagioclase was approximately 8.3% lower and 5% higher than that without exposure to thermal treatment, respectively. On the other hand, our nanoindentation tests showed that, for plagioclase, the reduced modulus increased by 3.8%, and hardness decreased by 7.8%, after thermal treatment. Except for impurities and inclusions, this discrepancy could be ascribed to the compositional variation of plagioclase and the roughness difference of indentation area. The elastic modulus of plagioclase varied with its chemical composition, since the exchange of Ca^{2+} for Na^+ leads to a change in Al:Si ratio (ranging from albite ($NaSi_3AlO_8$) to anorthite ($CaSi_2Al_2O_8$)) (Brown et al. 2016). Furthermore, the roughness of the indentation region significantly affects the nanoindentation test results (Majumdar et al. 2008). The lattice planes of quartz, amphibole, and plagioclase after thermal treatment were lower than those prior to thermal treatment (Figs. 15, 16 and 17, respectively). This could explain why their mechanical properties increased during cooling. For plagioclase, the spacing of lattice planes after thermal treatment cannot fully recover to the initial one at RT, probably due to the decomposition reactions (Fig. 19) and the irreversible phase transitions mentioned above. The causation of the reduced modulus decline of amphibole below 400 °C during cooling requires further investigation. In contrast, the lattice plane spacing of quartz after thermal treatment was close to that without exposure to thermal treatment. This explained the less significant reduction of mechanical properties for quartz than plagioclase. However, the mechanical properties of biotite decreased as temperature decreased. The cracks along the cleavage of biotite were found to expand obviously (Fig. 22) after thermal treatment. As noted above, the mechanical properties of biotite were dominated by the spacing of cleavages.

Therefore, the interlayered interaction strengthening leads to enhancement of the mechanical properties of biotite during cooling, even if its lattice planes tended to contract after cooling down (Fig. 18).

4.3 Implications for Macroscopic Mechanical Properties

During heating and cooling, the mechanical properties of minerals at microscale could influence those of granites at macroscale through thermally-induced microcracks. The mismatch between thermal expansion coefficients of minerals leads to thermally-induced microcracks during heating (Kranz 1983; Zhao 2016), as shown in Figs. 12 and 13.

The generation of these thermal microcracks can be divided into microcracks induced during heating [Fig. 14a] and those induced during cooling [Fig. 14b]. In addition, thermal stress can shrink pre-existing cracks, as illustrated in Fig. 14c. The pre-existing microcracks were reported to close due to thermal stress at low temperature during heating. The initiation of thermal microcracks occurred as thermal stress overcame the strength of mineral grains (Jansen et al. 1993). For instance, the thermal stress reached the tensile strength of the mineral, leading to microcracks (Yu et al. 2015). Ghasemi et al. (2020) concluded that the generation of microcracks in each mineral for granite was affected by the elastic modulus of the mineral. Their study suggested that biotite can absorb stress through deformation without initiating microcracks since biotite has the lowest elastic modulus (Fig. 6). Furthermore, the greater the elastic modulus difference between two mineral grains, the easier it is to generate boundary cracks (Ghasemi et al. 2020). The relation between the mineral elastic modulus and thermal stress could be established through a simplified thermomechanical model (Wang et al. 1989), i.e., thermal stress σ can be expressed by:

$$\sigma = E\Delta\alpha\Delta T \tag{9}$$

where E is the geometric mean of moduli of the two adjacent minerals; $\Delta\alpha$ is the thermal expansion contrast; and ΔT is the temperature change. Therefore, our measured mechanical

properties of minerals could, to a certain extent, predict the initiation or propagation of thermal microcracks during heating or cooling. Moreover, the initiation or closure of those thermal microcracks controlled the elastic modulus and mechanical strength of granites (Zhang et al. 2020; Wong et al. 2020). The correlation between the micromechanical properties of minerals and macromechanical properties of rocks could also be established via modeling. The real-time measured micromechanical properties can be used as inputs for numerical simulations at mesoscale or macroscale under heating and cooling conditions. Numerical methods based on thermo-mechanical coupled models were commonly used to investigate thermal effects on macroscopic mechanical properties. The constitutive relationships at microscale, however, were usually either simplified or established based on empirical formulas in these modelings (Zhao 2016). As a consequence, the simulated results may better reflect the actual situation if the measured micromechanical properties were entered into the numerical models.

5 Conclusion

In this study, the micromechanical properties of four common minerals in granites, i.e., quartz, plagioclase, amphibole, and biotite, were characterized in real time during the heating–cooling cycle. Changes in the microstructure of the minerals and variation of morphology during the thermal cycle were investigated. Thermal analysis based on coupled TG-FTIR was performed to examine the decomposition and chemical reactions during heating. On the basis of the above experimental results, the mechanisms of thermal effects on the mechanical properties of minerals and implications of the microscopic mechanical properties were discussed. The main conclusions are as follows:

(1) The micromechanical properties of quartz generally decreased during the heating processes and increased at the cooling stage. Its reduced modulus and hardness decreased by 12.6% and 21.6% at 500 °C, respectively. After cooling down to RT, the reduced modulus and hardness increased by 1.8% and 13.6%, respectively. The internal strain relaxation and atomic disorder alteration during the $\alpha - \beta$ transition of quartz contributed to the reduction of the mechanical properties of quartz. During the cooling process, the recovery of its lattice planes led to the increase of mechanical properties.

(2) During the heating process, the hardness of plagioclase generally decreased with temperature. The hardness decreased by approximately 13% at 500 °C. In contrast, its reduced modulus first increased below approximately 300 °C (3.8%), and then decreased. During the cooling process, the hardness of plagioclase showed

Table 4 The result of UCS tests

Parameter	Specimen ID			Mean	Standard deviation
	BM-01	BM-02	BM-03		
Peak stress (MPa)	116.44	221.43	120.89	152.92	59.38
Peak strain (mm mm^{-1})	1.070	0.997	0.939	1.002	0.066
Elastic modulus (GPa)	14.26	28.17	18.12	20.18	7.19
Poisson's ratio (-)	0.158	0.076	0.488	0.240	0.218

a significant increase, while its reduced modulus increased slightly. After exposure to the heating–cooling treatment, the hardness of plagioclase decreased by 7.9%, while its reduced modulus increased by 3.1%. The lattice spacing of plagioclase generally increased with temperature, resulting in improvement of its reduced modulus. However, the displacive phase transition of plagioclase that occurred at approximately (200 to 300)°C altered the crystallinity of plagioclase, which decreased the reduced modulus. Due to the water decomposition in plagioclase at high temperature and the irreversible phase transformation, the mechanical properties of plagioclase cannot recover completely after cooling down to RT.

(3) The reduced modulus and hardness of amphibole diminished with temperature during heating due to the dehydration reaction. However, the hardness of amphibole was more sensitive to high temperatures than the reduced modulus (i.e., the hardness and reduced modulus at 500 °C reduced by 5.6% and 23.4%, respectively, compared with those at RT). The hardness of amphibole increased during cooling. Its reduced modulus, however, increased before cooling down to 400 °C, and then decreased. After the cyclic heating–cooling treatment, the hardness and reduced modulus of amphibole decreased by 8.7% and 14.3%, respectively.

(4) The mechanical properties of biotite increased significantly during heating, and reduced during cooling. At the maximum heating temperature, the reduced modulus and hardness of biotite increased by 62.3% and 105.5%, respectively. After cooled down to RT, an increase of 41.8% and 65.6% was found for reduced modulus and hardness, respectively. The spacing of the open cracks along cleavages controlled the mechanical properties of biotite. The weakening of interlayered interactions due to the shrinkage of the open cracks enhanced the mechanical properties during the heating process, although its lattice planes increased. At the cooling stage, the expansion of open cracks resulted in the decrease of mechanical properties. The expansion during cooling, however, cannot offset the shrinkage during heating because the
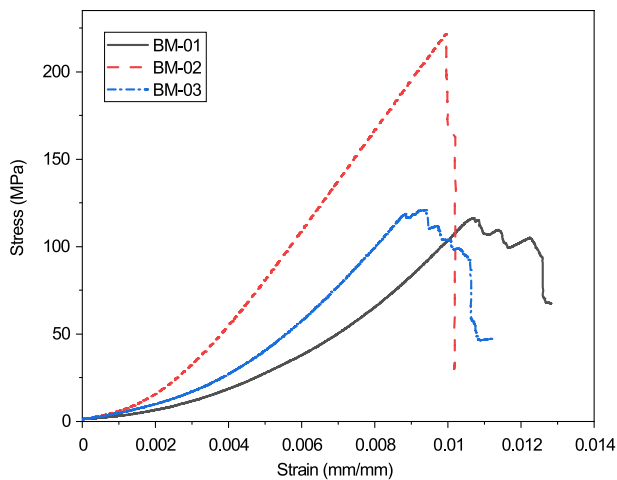
Fig. 23 Stress-strain curves of the specimens

thermal decomposition of combined water and structural water altered its internal structure.

(5) The measured micromechanical properties of minerals were correlated to the mechanical properties of rocks at macroscale through the thermally-induced microcracks. This is because the initiation and propagation of the thermal-included cracks could be affected by the micromechanical properties of the mineral. Moreover, the thermal cracks controlled the macromechanical properties of rocks. Therefore, the obtained micromechanical properties could be utilized to predict the mechanical properties of rocks at macroscale in future works.

Appendix A UCS Testing

The detail of the uniaxial comprehensive strength (UCS) test is presented in this section.

Specimen Preparation

According to the size recommended by the international society for rock mechanics (ISRM) (Bieniawski and Bernede 1979), the diameter of UCS specimen was 25 mm, and the length was 50 mm. The two ends of each cylinder were ground for smoothness and parallel with each other.

Test Procedure

To obtain the UCS of the granite, an MTS-816 machine was employed. The specimens were loaded until failure under a displacement-control mode with a loading rate of 1×10^{-5} mm s^{-1}. As mentioned in Sect. 2.1, the rock specimens were obtained from the outcrop of the Gonghe Basin

in Qinghai, China, which was not readily available. Consequently, only three UCS tests were replicated.

Results

The experiment result of UCS tests is list in Table 4. Stress-strain curves of the specimens are shown in Fig 23.

References

Bieniawski Z, Bernede M (1979) Suggested methods for determining the uniaxial compressive strength and deformability of rock materials: Part 1. suggested method for determining deformability of rock materials in uniaxial compression. Int J Rock Mech Min Sci Geomech Abstr 16(2):138–140. https://doi.org/10.1016/0148-9062(79)91451-7

Bragg WL, Gibbs RE (1925) The structure of α and β quartz. Proc R Soc Lond 109(751):405–427

Brown JM, Abramson EH (2016) Elasticity of calcium and calcium-sodium amphiboles. Phys Earth Planet Inter 261:161–171

Brown JM, Angel RJ, Ross NL (2016) Elasticity of plagioclase feldspars. J Geophys Res Solid Earth 121(2):663–675. https://doi.org/10.1002/2015JB012736

Bruker (2021) Software: Amics automated mineralogy system for sem bruker. https://www.bruker.com/en/products-and-solutions/elemental-analyzers/eds-wds-ebsd-SEM-Micro-XRF/software-amics-automated-mineralogy-system.html. (Accessed on 09 Nov 2021)

Chen YL, Wang SR, Ni J, Azzam R, Fernandez-Steeger TM (2017) An experimental study of the mechanical properties of granite after high temperature exposure based on mineral characteristics. Eng Geol 220:234–242. https://doi.org/10.1016/j.enggeo.2017.02.010

Duffy TS, Vaughan MT (1988) Elasticity of enstatite and its relationship to crystal structure. J Geophys Res Solid Earth 93(B1):383–391. https://doi.org/10.1029/JB093iB01p00383

Fan Z, Wei H, Han-qun G, Da-wei H, Qian S, Jian-fu S (2018) Nanoindentation tests on granite after heat treatment. Rock Soil Mech 39:235–243

Fischer-Cripps AC, Nicholson D (2004) Nanoindentation. Mechanical engineering series. Appl Mech Rev 57(2):B12–B12

Fröhlich F, Grau P, Grellmann W (1977) Performance and analysis of recording microhardness tests. Phys Status Solidi 42(1):79–89

Ghasemi S, Khamehchiyan M, Taheri A, Nikudel MR, Zalooli A (2020) Crack evolution in damage stress thresholds in different minerals of granite rock. Rock Mech Rock Eng 53:1163–1178. https://doi.org/10.1007/s00603-019-01964-9

Gibbs RE (1925) The variation with temperature of the intensity of reflection of x-rays from quartz and its bearing on the crystal structure. Proc R Soc Lond 107(743):561–570

Griffiths L, Lengliné O, Heap M, Baud P, Schmittbuhl J (2018) Thermal cracking in westerly granite monitored using direct wave velocity, coda wave interferometry, and acoustic emissions. J Geophys Res Solid Earth 123:2246–2261. https://doi.org/10.1002/2017JB015191

Hertz H (1881) On the contact of elastic solids. Z Reine Angew Math 92:156–171

Huang ZH, Gandais M, Gaboriaud RJ (1985) Microhardness of feldspar single crystals (or98 and an58) as a function of temperature. Bull Minéral 108(6):835–841

Jansen D, Carlson S, Young R, Hutchins D (1993) Ultrasonic imaging and acoustic emission monitoring of thermally induced microcracks in lac du bonnet granite. J Geophys Res Solid Earth 98(B12):22231–22243

Kimizuka H, Kaburaki H, Kogure Y (2003) Molecular-dynamics study of the high-temperature elasticity of quartz above the α-β phase transition. Phys Rev B 67:1–7. https://doi.org/10.1103/PhysRevB.67.024105

Kobchenko M, Panahi H, Renard F, Dysthe DK, Malthe-Srenssen A, Mazzini A, Scheibert J, Jamtveit B, Meakin P (2011) 4D imaging of fracturing in organic-rich shales during heating. J Geophys Res Solid Earth 116(12):1–9. https://doi.org/10.1029/2011JB008565

Kranz RL (1983) Microcracks in rocks: a review. Tectonophysics 100(1–3):449–480

Lakshtanov DL, Sinogeikin SV, Bass JD (2007) High-temperature phase transitions and elasticity of silica polymorphs. Phys Chem Miner 34(1):11–22

Lanin ES, Sone H, Yu Z, Liu Q, Wang B (2021) Comparison of biotite elastic properties recovered by spherical nanoindentations and atomistic simulations - influence of nanoscale defects in phyllosilicates. J Geophys Res Solid Earth 126(8):e2021JB021902. https://doi.org/10.1029/2021JB021902

Li N, Zhang S, Ma X, Zou Y, Li S, Zhang Z (2020) Thermal effect on the evolution of hydraulic fracture conductivity: an experimental study of enhanced geothermal system. J Pet Sci Eng 187:106814. https://doi.org/10.1016/j.petrol.2019.106814

Liu K, Ostadhassan M, Bubach B (2016) Applications of nanoindentation methods to estimate nanoscale mechanical properties of shale reservoir rocks. J Nat Gas Sci Eng 35:1310–1319. https://doi.org/10.1016/j.jngse.2016.09.068

Liu W, Yang Y, Xia Q, Ye Y, Wang Z, Zhang P, Li G (2018) Water decreases displacive phase transition temperature in alkali feldspar. Eur J Mineral 30:1071–1081. https://doi.org/10.1127/ejm/2018/0030-2775

Luo S, Kim D, Wu Y, Li Y, Wang D, Song J, DeGroot DJ, Zhang G (2021) Big data nanoindentation and analytics reveal the multistaged, progressively-homogenized, depth-dependent upscaling of rocks' properties. Rock Mech Rock Eng 54:1501–1532. https://doi.org/10.1007/s00603-020-02337-3

Ma X, Wang G, Hu D, Liu Y, Zhou H, Liu F (2020) Mechanical properties of granite under real-time high temperature and three-dimensional stress. Int J Rock Mech Min 136:104521. https://doi.org/10.1016/j.ijrmms.2020.104521

Majumdar P, Singh S, Chakraborty M (2008) Elastic modulus of biomedical titanium alloys by nano-indentation and ultrasonic techniques–a comparative study. Mater Sci Eng A 489:419–425. https://doi.org/10.1016/J.MSEA.2007.12.029

Maruvanchery V, Kim E (2020) Mechanical characterization of thermally treated calcite-cemented sandstone using nanoindentation, scanning electron microscopy and automated mineralogy. Int J Rock Mech Min Sci 125:104158. https://doi.org/10.1016/j.ijrmms.2019.104158

Mavko G, Mukerji T, Dvorkin J (2020) The rock physics handbook. Cambridge University Press

Newey D, Wilkins M, Pollock H (1982) An ultra-low-load penetration hardness tester. J Phys E Sci Instr 15(1):119

Noyan IC, Cohen JB (2013) Residual stress: measurement by diffraction and interpretation. Springer

Ohno I (1995) Temperature variation of elastic properties of α-quartz up to the α-β transition. J Phys Earth 43(2):157–169

Ohno I, Harada K, Yoshitomi C (2006) Temperature variation of elastic constants of quartz across the $\alpha - \beta$ transition. Phys Chem Miner 33:1–9. https://doi.org/10.1007/s00269-005-0008-3

Oliver WC, Pharr GM (1992) An improved technique for determining hardness and elastic modulus using load and displacement sensing indentation experiments. J Mater Res 7(6):1564–1583

Oliver WC, Pharr GM (2004) Measurement of hardness and elastic modulus by instrumented indentation: advances in understanding and refinements to methodology. J Mater Res 19(1):3–20

Pathak S, Kalidindi SR (2015) Spherical nanoindentation stress-strain curves. Mater Sci Eng R Rep 91:1–36. https://doi.org/10.1016/j.mser.2015.02.001

Pethicai J, Hutchings R, Oliver WC (1983) Hardness measurement at penetration depths as small as 20 nm. Philos Mag A 48(4):593–606

Riecker RE, Rooney TP (1969) Water-induced weakening of hornblende and amphibolite. Nature 224(5226):1299

Shao S, Ranjith P, Wasantha P, Chen B (2015) Experimental and numerical studies on the mechanical behaviour of Australian strathbogie granite at high temperatures: An application to geothermal energy. Geothermics 54:96–108. https://doi.org/10.1016/j.geothermics.2014.11.005

Shim S, Bei H, George EP, Pharr GM (2008) A different type of indentation size effect. Scr Mater 59(10):1095–1098

Shukla P, Kumar V, Curtis M, Sondergeld CH, Rai CS (2013) Nanoindentation studies on shales. In: 47th U.S. Rock mechanics/geomechanics symposium. OnePetro. San Francisco, California. All Days. https://onepetro.org/ARMAUSRMS/proceedings-pdf/ARMA13/All-ARMA13/ARMA-2013-578/1527543/arma-2013-578.pdf

Su Y, Bhunia S, Xu S, Chen A, Reddy CM, Cai T (2021) Structure-thermomechanical property correlation in polymorphic molecular crystals probed by the nanoindentation technique. Chem Mater 33(12):4821–4829. https://doi.org/10.1021/acs.chemmater.1c00584

Teich-McGoldrick SL, Greathouse JA, Cygan RT (2012) Molecular dynamics simulations of structural and mechanical properties of muscovite: pressure and temperature effects. J Phys Chem C 116:15099–15107. https://doi.org/10.1021/jp303143s

Tian WL, Yang SQ, Elsworth D, Wang JG, Li XZ (2020) Permeability evolution and crack characteristics in granite under treatment at high temperature. Int J Rock Mech Min Sci 134:104461. https://doi.org/10.1016/j.ijrmms.2020.104461

Tiskatine R, Eddemani A, Gourdo L, Abnay B, Ihlal A, Aharoune A, Bouirden L (2016) Experimental evaluation of thermo-mechanical performances of candidate rocks for use in high temperature thermal storage. Appl Energy 171:243–255. https://doi.org/10.1016/j.apenergy.2016.03.061

Tomac I, Sauter M (2018) A review on challenges in the assessment of geomechanical rock performance for deep geothermal reservoir development. Renew Sustain Energy Rev 82(October 2017):3972–3980. https://doi.org/10.1016/j.rser.2017.10.076

Tucker M, Keen D, Dove M (2001) A detailed structural characterization of quartz on heating through the α-β phase transition. Mineral Mag 65:489–507. https://doi.org/10.1180/0026461017 50377524

Tutti F, Lazor P (2000) High-temperature study and thermal expansion of phlogopite. Phys Chem Miner 27(9):599–603. https://doi.org/10.1007/s002690000098

Vázquez P, Shushakova V, Gómez-Heras M (2015) Influence of mineralogy on granite decay induced by temperature increase: experimental observations and stress simulation. Eng Geol 189:58–67. https://doi.org/10.1016/j.enggeo.2015.01.026

Vyzhva SA, Prodayvoda GT, Vyzhva AS (2014) Elastic properties of some clay minerals. Nafta-Gaz 70(11):743–756

Wang HF, Bonner BP, Carlson SR, Kowallis BJ, Heard HC (1989) Thermal stress cracking in granite. J Geophys Res Solid Earth 94(B2):1745–1758. https://doi.org/10.1029/JB094iB02p01745

Winter JK, Okamura FP, Ghose S (1979) A high-temperature structural study of high albite, monalbite, and the analbite → monalbite phase transition. Am Mineral 64(3–4):409–423

Wong LNY, Zhang Y, Wu Z (2020) Rock strengthening or weakening upon heating in the mild temperature range? Eng Geol 272:105619

Wu SJ, Chin PC, Liu H (2019) Measurement of elastic properties of brittle materials by ultrasonic and indentation methods. Appl Sci. https://doi.org/10.3390/app9102067

Wu X, Huang Z, Cheng Z, Zhang S, Song H, Zhao X (2019) Effects of cyclic heating and ln_2-cooling on the physical and mechanical properties of granite. Appl Therm Eng 156:99–110

Yang SQ, Ranjith P, Jing HW, Tian WL, Ju Y (2017) An experimental investigation on thermal damage and failure mechanical behavior of granite after exposure to different high temperature treatments. Geothermics 65:180–197. https://doi.org/10.1016/j.geothermics.2016.09.008

Yang Y, Wang Z, Tian Z, Xia Q, Li G (2016) High-temperature phase transition and local structure of a hydrous anorthoclase. Phys Chem Miner 43:111–118. https://doi.org/10.1007/s00269-015-0778-1

Yin T, Li Q, Li X (2019) Experimental investigation on mode i fracture characteristics of granite after cyclic heating and cooling treatments. Eng Fract Mech 222:106740. https://doi.org/10.1016/j.engfracmech.2019.106740

Yin T, Shu R, Li X, Wang P, Liu X (2016) Comparison of mechanical properties in high temperature and thermal treatment granite. Trans Nonferrous Met Soc China 26(7):1926–1937. https://doi.org/10.1016/S1003-6326(16)64311-X

Yu Q, Ranjith P, Liu H, Yang T, Tang S, Tang CA, Yang S (2015) A mesostructure-based damage model for thermal cracking analysis and application in granite at elevated temperatures. Rock Mech Rock Eng 48(6):2263–2282

Zhang Y, Guo-Feng Z, Li Q (2020) Acoustic emission uncovers thermal damage evolution of rock. Int J Rock Mech Min Sci 132:104388. https://doi.org/10.1016/j.ijrmms.2020.104388

Zhang J, Hu L, Pant R, Yu Y, Wei Z, Zhang G (2013) Effects of interlayer interactions on the nanoindentation behavior and hardness of 2:1 phyllosilicates. Appl Clay Sci 80–81:267–280. https://doi.org/10.1016/j.clay.2013.04.013

Zhang Z, Ma B, Ranjith P, Yang S, Zhou L (2020) Indications of risks in geothermal systems caused by changes in pore structure and mechanical properties of granite: an experimental study. Bull Eng Geol Environ 79:5399–5414. https://doi.org/10.1007/s10064-020-01901-z

Zhang G, Wei Z, Ferrell RE, Guggenheim S, Cygan RT, Luo J (2010) Evaluation of the elasticity normal to the basal plane of non-expandable 2:1 phyllosilicate minerals by nanoindentation. Am Mineral 95:863–869. https://doi.org/10.2138/AM.2010.3398

Zhang M, Wruck B, Barber AG, Salje E, Carpenter M (1996) Phonon spectra of alkali feldspars: phase transitions and solid solutions. Am Mineral 81(1–2):92–104

Zhao Z (2016) Thermal influence on mechanical properties of granite: a microcracking perspective. Rock Mech Rock Eng 49(3):747–762

Zhao J, Zhang D, Wu T, Tang H, Xuan Q, Jiang Z, Dai C (2019) Multiscale approach for mechanical characterization of organic-rich shale and its application. Int J Geomech 19(1):04018180

Zhou XP, Li GQ, Ma HC (2020) Real-time experiment investigations on the coupled thermomechanical and cracking behaviors in granite containing three pre-existing fissures. Eng Fract Mech 224:106797. https://doi.org/10.1016/j.engfracmech.2019.106797

Zhu W, Hughes JJ, Bicanic N, Pearce CJ (2007) Nanoindentation mapping of mechanical properties of cement paste and natural rocks. Mater Charact 58(11):1189–1198. https://doi.org/10.1016/j.matchar.2007.05.018

Zhu Z, Ranjith PG, Tian H, Jiang G, Dou B, Mei G (2021) Relationships between p-wave velocity and mechanical properties of granite after exposure to different cyclic heating and water cooling treatments. Renew Energy 168:375–392. https://doi.org/10.1016/j.renene.2020.12.048

Zhu Z, Tian H, Mei G, Jiang G, Dou B (2020) Experimental investigation on physical and mechanical properties of thermal cycling granite by water cooling. Acta Geotech 15:1881–1893. https://doi.org/10.1007/s11440-019-00898-4